

## Article

# Quantitative Description of Pore and Fracture Distribution Heterogeneity Using Mercury Removal Curve and Applicability of Fractal Models

Huasheng Chong <sup>1</sup>, Xiao Liu <sup>2</sup>, Danyang Xi <sup>3,\*</sup> , Junjian Zhang <sup>4</sup> , Veerle Vandeginste <sup>5</sup> , Dongdong Wang <sup>4</sup> and Peng Yao <sup>4</sup>

<sup>1</sup> Tengzhou Guozhuang Mining Co., Ltd., Zaozhuang 277500, China; chonghuasheng@tzgzkj.net

<sup>2</sup> Fifth Exploration Team of Shandong Coal Geological Bureau, Jinan 250100, China; 15253839876@163.com

<sup>3</sup> School of Resources and Earth Science, China University of Mining and Technology, Xuzhou 221116, China

<sup>4</sup> College of Earth Sciences & Engineering, Shandong University of Science and Technology, Qingdao 266590, China; skd996457@sdust.edu.cn (J.Z.); wdd02\_1@163.com (D.W.); yaopeng202209@163.com (P.Y.)

<sup>5</sup> Department of Materials Engineering, KU Leuven, Campus Bruges, 8200 Bruges, Belgium; veerle.vandeginste@kuleuven.be

\* Correspondence: dyxi@cumt.edu.cn

**Abstract:** Many studies have used fractal theory to characterize pore structure distribution heterogeneity through mercury intake curves. However, there is relatively little research on the fractal model calculation of mercury removal curves. In this study, a high-pressure mercury intrusion test is used to describe the pore and fracture distribution heterogeneity (PFDH). The fractal physical meaning of the mercury removal curve was determined by calculating the change in the curve's fractal dimension value. The results are as follows. (1) According to mercury removal efficiency and porosity, samples can be divided into types A (mercury removal efficiency above 35%) and B (mercury removal efficiency below 35%). In general, type A sample belongs to micro-pore-developed types, and type B samples belong to the macro-pore-developed type. (2) The Menger model (M) represents the complexity of a specific surface area, while the Sierpinski model (S) represents the roughness of the pore volume. Among all the samples, the lower-pore-volume region controls PFDH. (3) According to the calculation results of the single fractal model, it can be seen that the PFDH of type B is stronger than that of type A, which is similar to the results of mercury intrusion. According to the calculation structure of the multifractal model, it can be seen that the volume distribution heterogeneity of type B under various pores is significantly stronger than that of type A. This is opposite to the result of mercury injection. (4)  $D_M$  has a relationship with the pore volume percentage at different stages, so the M model at the mercury inlet stage can better characterize PFDH at the mercury inlet stage.

**Keywords:** unconventional reservoirs; fractal dimension; pore diameter distribution; adsorption; seepage



**Citation:** Chong, H.; Liu, X.; Xi, D.; Zhang, J.; Vandeginste, V.; Wang, D.; Yao, P. Quantitative Description of Pore and Fracture Distribution Heterogeneity Using Mercury Removal Curve and Applicability of Fractal Models. *Processes* **2024**, *12*, 917. <https://doi.org/10.3390/pr12050917>

Academic Editor: Qingbang Meng

Received: 1 April 2024

Revised: 27 April 2024

Accepted: 27 April 2024

Published: 30 April 2024



**Copyright:** © 2024 by the authors. Licensee MDPI, Basel, Switzerland. This article is an open access article distributed under the terms and conditions of the Creative Commons Attribution (CC BY) license (<https://creativecommons.org/licenses/by/4.0/>).

## 1. Introduction

Coal reservoirs are dominated by fracture and nano-micro-pores, and as a channel for gas and water migration, the development of fractures directly affects gas and water migration. Adsorption pores generally develop pores whose pore diameter is smaller than 100 nm, and their large specific surface area provides broad space for methane molecule adsorption. Therefore, CBM production potential is determined by the pore fracture structure system [1–3]. The coal reservoir exhibits a distinct dual porosity and single permeability model. Dual pores include pores and fractures, while pores include adsorption pores and seepage pores. Among them, adsorption pores mainly refer to pores with a pore size less than 100 nm. The large specific surface area of these pores provides a wide range of methane adsorption sites, mainly controlling the methane adsorption

characteristics. Seepage pores mainly refer to pores with a pore size greater than 100 nm. The large pore volume of these pores provides a wide range of methane storage space, mainly controlling the gas water migration channel and affecting the permeability of the gas water two-phase flow.

At present, photoelectric observation technology, gas adsorption technology, fluid intrusion technology, and three-dimensional structure reconstruction technology are used to study the pore structure of coal reservoirs [4,5]. On this basis, the Hodot partition scheme (micro-pore, <100 nm; meso-pore, 100–1000 nm; macro-pore, >1000 nm) and IUPAC partition scheme (micro-pore, <2 nm; meso-pore, 2–50 nm; macro-pore, >50 nm) are used in pore description [6,7]. Generally, pores larger than 100 nm are classified as percolation pores, and their structure influences the percolation and migration of coalbed methane [8–11].

Compared with other experimental methods, the high-pressure mercury intrusion test (HPMI) can characterize nano-pores by measuring the mercury injection volume under different injection pressures to calculate the pore volume, specific surface area, and other parameters [12–14]. This technique has become one of the most commonly used methods for studying unconventional reservoir structures due to its speed, simplicity, and low-cost advantages. On this basis, many studies have examined the shape and volume of mercury injection curves and their effects on pore type, pore size distribution, and dynamic changes in porosity [15,16]. However, there are relatively few studies on the mercury removal curve (MRC), and the mercury removal efficiency (MRE) is taken as the research content. Compared with the mercury inlet curve (MIC), the MRC can characterize the migration of gas and water [17,18], covering a larger range of pore diameters, thus more comprehensively describing the pore structure of rocks. It is more sensitive to the heterogeneity of rock pore space and can better reflect the distribution of pores inside the rock. The MRC can also reflect the connectivity between pores, that is, whether a connected network is formed in the pore space, which is of great significance for understanding the migration of fluids in rocks [19,20]. Therefore, MRC needs to be studied.

There are many problems in studying pore structure using traditional geometric methods, such as the inability of this theory to achieve the quantitative characterization of the pore structure. Therefore, the fractal dimension value by using the HPMI mercury intrusion curve has become the main method to characterize pore and fracture structure distribution heterogeneity (PFDH) in unconventional reservoirs. Fractal models include the Menger (M) model, the thermodynamic (T) model, and the multifractal model. The data from the above fractal model are all from MIC, and HPMI is discussed by calculating the fractal dimension [21–23]. However, whether MRC is fractal and its effect on the changes of porosity and permeability remain to be discussed.

In this study, 14 coal samples are collected from the Taiyuan and Shanxi Formation in Ningdong Coalfield. The pore distributions of the samples are determined by using HPMI, and pore types are determined based on the pore volume and specific surface area. Based on this, the quantitative description of pore and fracture distribution heterogeneity is described by using mercury inlet and removal curves. Four fractal models are employed to quantitatively characterize the fractal properties of the MRC and MIC. The correlation between fractal dimension values by using MRC and MIC is determined. Subsequently, the correlation between the fractal dimension of mercury removal and pore structure parameters is investigated. The physical significance of fractal characteristics by using mercury removal curves is elucidated.

## 2. Experimental Testing and Fractal Theory

### 2.1. Sample Preparation and Experimental Testing

In this study, 14 coal samples are collected from Taiyuan and Shanxi Formation in Ningdong Coalfield. The study area is situated in the central segment of a fold thrust belt on the western perimeter of the Ordos Basin, and its formation and evolution are clearly controlled by the coupling effect between the Helan Mountains Liupanshan structural

belt and the Ordos Basin. The Carboniferous Permian formation comprises coal-bearing sedimentary structures that developed atop the ancient weathering crust of the Ordovician. The Jurassic formation, on the other hand, consists of terrestrial coal-bearing sedimentary structures that formed within inland lake basins. The Carboniferous Permian coal-bearing strata comprise the Taiyuan Formation and Shanxi Formation, while the Jurassic coal-bearing strata are represented by the Yan'an Formation. Among them, Taiyuan Formation developed a coastal carbonate shelf sedimentary system, while the Shanxi Formation developed river and delta sedimentary systems. The Taiyuan Formation and Shanxi Formation have a total of 5–27 coal seams, with an average thickness of 8.98–21.21 m. The degree of coal metamorphism is middle-rank coal. The coal quality has characteristics, such as low ash to medium ash, medium to low sulfur, low phosphorus, and medium to low chlorine [24]. The basic information of the sample is shown in Table 1.

**Table 1.** Basic information on all the samples.

| Sample Number | Porosity (%) | Permeability ( $10^{-3} \mu\text{m}^2$ ) | Mercury Removal Efficiency (%) | Percent Pore Volume (%) |             |         |
|---------------|--------------|--|--------------------------------|-------------------------|-------------|---------|
|               |              |  |                                | 1000~10,000 nm          | 100~1000 nm | <100 nm |
| 4-15          | 8.660        | 1.510                                    | 43.470                         | 0.082                   | 0.115       | 0.607   |
| 2-4           | 7.190        | 1.210                                    | 46.987                         | 0.395                   | 0.226       | 0.300   |
| 3-18          | 3.970        | 0.250                                    | 44.954                         | 0.279                   | 0.313       | 0.320   |
| 3-8           | 8.750        | 1.610                                    | 46.737                         | 0.437                   | 0.355       | 0.161   |
| L2-15         | 4.450        | 0.120                                    | 39.853                         | 0.305                   | 0.356       | 0.253   |
| L2-14         | 4.280        | 0.130                                    | 40.570                         | 0.302                   | 0.369       | 0.252   |
| L2-8          | 4.360        | 0.130                                    | 39.641                         | 0.311                   | 0.378       | 0.252   |
| L2-3          | 7.920        | 0.120                                    | 41.312                         | 0.029                   | 0.618       | 0.291   |
| 8-7           | 5.960        | 0.100                                    | 34.648                         | 0.017                   | 0.726       | 0.203   |
| L2-20         | 9.630        | 0.700                                    | 29.982                         | 0.607                   | 0.309       | 0.051   |
| L2-19         | 10.050       | 1.470                                    | 27.547                         | 0.698                   | 0.236       | 0.035   |
| 4-24          | 8.120        | 1.000                                    | 33.716                         | 0.304                   | 0.168       | 0.440   |
| L2-2          | 8.580        | 0.560                                    | 25.024                         | 0.333                   | 0.441       | 0.192   |
| L2-12         | 10.440       | 1.960                                    | 31.130                         | 0.575                   | 0.265       | 0.126   |

A cylindrical sample of  $15 \times 15 \times 15$  cm was wrapped in fresh sample bags and then sent to laboratory for testing. Firstly, mortar was used to grind the sample into powder and we conducted microscopic and industrial component testing. Secondly, the sample was polished and dried at  $60^\circ\text{C}$  for 48 h. The pore rupture experiment was carried out using a 9520 mercury injection instrument. The maximum experimental pressure was 100 MPa, the aperture measurement range was  $0.069\text{--}144 \mu\text{m}$ , and the test temperature was normal temperature. This technique works on intrusion of mercury in the pore space at high pressures. The intrusion pressure is used to estimate the pore radius, and the intruded volume is used to estimate the pore volume. The pore size limits from MIP were determined using the empirical Washburn equation [25,26]:

$$r = \frac{-2\sigma \cos \theta}{p} \quad (1)$$

where  $p$  is the intrusion pressure, MPa;  $\sigma$  is the interfacial tension of mercury,  $0.484 \text{ N/m}$ ;  $\theta$  is the mercury–coal contact angle,  $140^\circ$ ; and  $r$  is the pore radius, nm.

Assuming the pores are cylindrical, the specific surface area (SSA) of a pore can be calculated using Equation (2).

$$S = -\frac{1}{\sigma \cos \theta} \int_0^V P dV \quad (2)$$

where  $S$  is the SSA of pore,  $\text{m}^2/\text{g}$ ;  $V$  is the cumulative intrusion volume,  $\text{cm}^3/\text{g}$ .

## 2.2. Fractal Theory

The capillary curve is obtained using high-pressure mercury intrusion testing methods, and this parameter has a significant impact on gas–water migration in the pore fracture system. The fractal model calculation based on high-pressure mercury intrusion testing has become one of the most important methods for quantitatively characterizing the heterogeneity of pore and fracture structure distribution. Fractal models mainly include two types, that is, single fractal and multi-models. Fractal models include the Menger (M) model, the Sierpinski model, the thermodynamic (T) model, and the multifractal model. M and S fractal models are the two most commonly used single fractal models. Relevant literature indicates that the M model characterizes pore volume distribution heterogeneity, while the S model characterizes the heterogeneity of pore-specific surface area distribution [27].

However, the above model only provides a simple description of the non-uniformity of pores and fracture by obtaining a single fractal dimension. The pore size distribution of coal reservoirs with strong heterogeneity exhibits fluctuations and jumps, and different pore size intervals exhibit different types of self-similarity, which also makes it difficult to achieve full-scale quantitative characterization of pore and fracture structures with a single fractal dimension value [26]. Differing from single fractal, multifractal can divide the aperture curve into multiple small regions with different singularities, studying the fractal characteristics of different regions in the form of small intervals, and, thereby, the fine structure of the pore fracture system of the entire unconventional reservoir is determined.

The Menger model (M model) is presented in Equation (3) [27]

$$\lg(dv/dp) \propto (D - 4)\lg(p) \quad (3)$$

where  $D_M$  is dimensionless fractal dimension;  $p$  is mercury inlet pressure, MPa;  $V$  is total mercury inlet volume,  $\text{cm}^3 \cdot \text{g}^{-1}$ .

The Sierpinski model (S model) is presented in Equation (4) [28]

$$\ln(v) = (3 - D)\ln(p - p_t) + \ln a \quad (4)$$

where  $V$  is mercury inlet volume, mL;  $P$  is mercury inlet pressure, Mpa;  $P_t$  is threshold pressure, MPa;  $D_S$  is fractal dimension;  $a$  is a constant.

$q \sim D(q)$  is a fundamental expression for describing the local characteristics of a multifractal. The calculation expression of  $D(q)$  is as follows [22,29,30]:

$$D(q) = \frac{\tau(q)}{q - 1} \quad (5)$$

where  $\tau(q)$  is the mass exponent function, and  $q$  is the order of statistical moment. For detailed information on the process, refer to the literature [11].

The fractal model's data are represented by MIC, and the fractal dimension of PFDH is analyzed through calculation. The potential fractality of MRC and its influence on variations in porosity and permeability will be examined. Using the MRC data from the same sample, the fractal dimensions of two individual fractal models and multifractal models will be computed. The disparity in fractality between MIC and MRC of the identical sample will be investigated.

## 3. Results and Discussion

### 3.1. Pore Distribution Characteristics by Using HPMI Test

Figure 1a shows that the mercury inlet volume is 0 when the pressure is smaller than 1 MPa. When the pressure is from 1 to 100 MPa, the MIC of some samples increases almost vertically, indicating that the micro-pores are widely developed. The MIC of most samples rose gently, indicating a balanced development of micro-pores and meso-pores. In the process of mercury removal, MRC is close to horizontal, and MRE is low, indicating that

the porosity is relatively smaller, and the connectivity between the pores and fracture is poor but the MRE is different. Based on differences in research objectives, sample types are classified according to porosity, MRE, and other factors. Figure 1a shows that all samples are classified as two types by using MRE and porosity. To better describe the pore structure, the pore is divided into macro-pores (1000~10,000 nm), seepage pores (100~1000 nm), and adsorption pores (<100 nm).

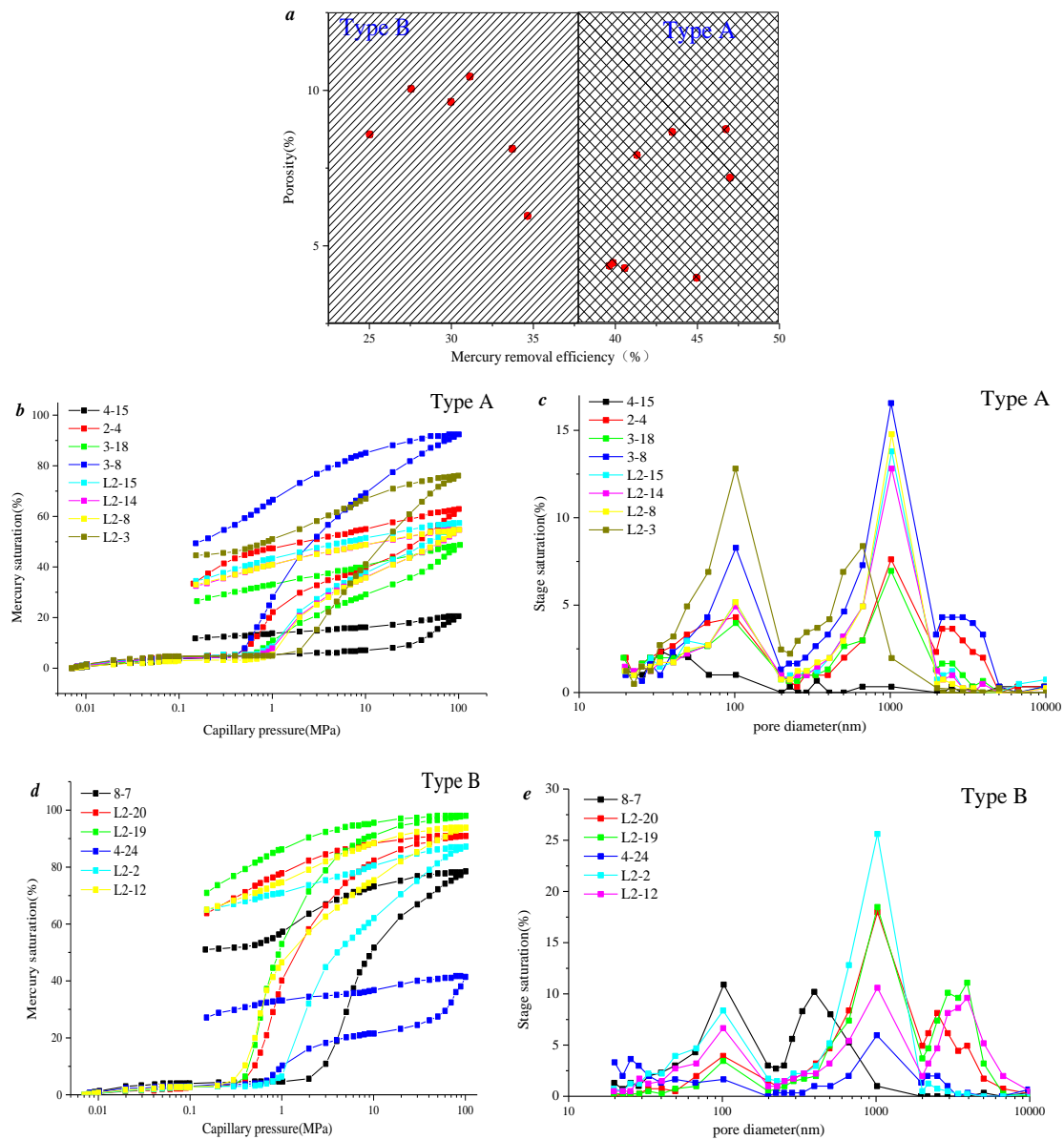


**Figure 1.** The inlet and outlet mercury curves and pore fracture distribution of all samples ((a), mercury removal efficiency vs. porosity; (b), mercury intrusive curve of type A; (c), pore size distribution of type A; (d), mercury intrusive curve of type B; (e), pore size distribution of type B).

Figure 1a illustrates that the MRE of type A is higher than that of type B, suggesting that type A is characterized by a large pore volume, MRE, and simple pore structure. This characteristic should be the focal point of future research. Figure 2 shows that the macro-pore volume percentage of type A is 30–45%, which is higher than that of type B, and the macro-pore volume of different types is different. The seepage pore volume percentage of type B is higher than that of type A, but the adsorption pore volume percentage of type A is a little different from that of type B. In general, type A develops macro-pores and type B develops adsorption pores (Figure 1).

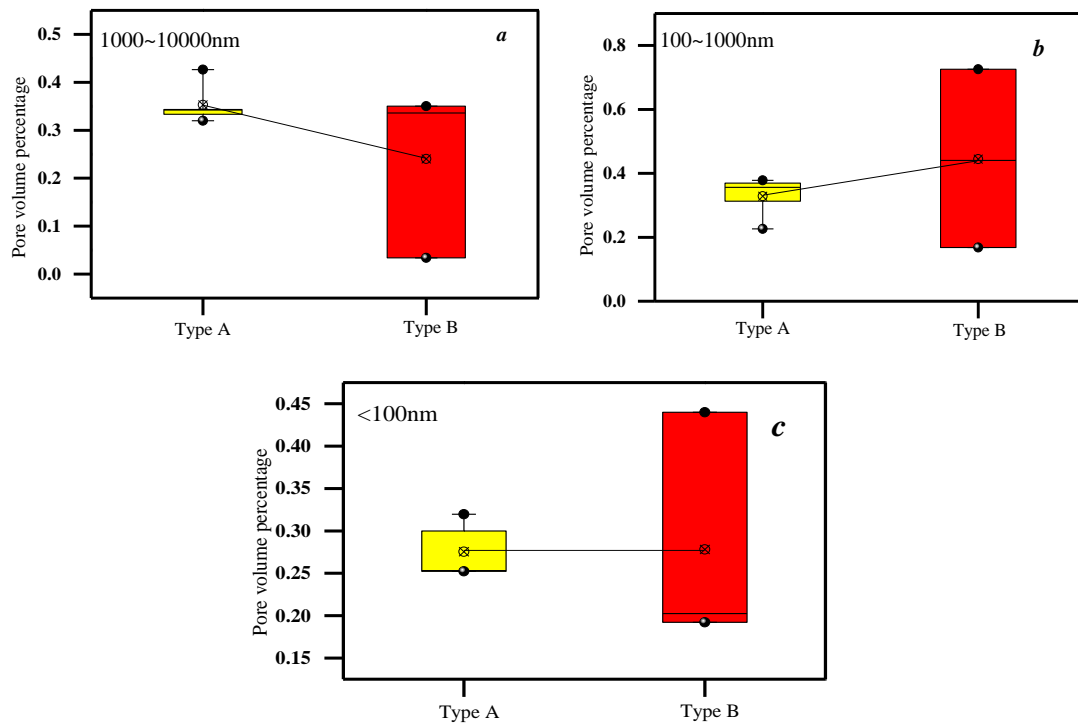


**Figure 2.** Pore distribution characteristics of different types of samples (a), 1000~10,000 of pore volume percentage of type A and B; (b), 100~1000 of pore volume percentage of type A and B; (c), <100 nm of pore volume percentage of type A and B.

### 3.2. Pore and Fracture Distribution Heterogeneity by Using Mercury Inlet Curve

$D_M$  can be determined by using the Menger model (Equation (1)). The fractal curve indicates that there is a linear negative correlation between  $\log p$  and  $\log (dv/dp)$ , indicating that the fractal characteristics of the mercury intrusion curve can be characterized using this model. The ranges of A-type linear fitting and  $D_M$  are 0.88 to 0.95 and 3.18 to 3.24, respectively. The linear fitting range and  $D_M$  of B-type samples are 0.85 to 0.89 and 3.17 to 3.24, respectively (Figure 3). Overall, there is a similarity in the  $D_M$  values between type A and type B, indicating that the heterogeneity of pore distribution in the two types of samples is relatively small.

The *Sierpinski* model calculation can calculate  $D_S$  (Equation (2)). The fractal curve shows that the linear relationship between  $\ln p$  and  $\ln v$  is positively correlated, which indicates that the linear relationship of this model can reflect the fractal characteristics. Thus, 0.91~0.94 is the range of A-type linear fitting, and 2.49~2.57 is the range of  $D_S$ ; 0.90~0.95 is the B-type linear fitting range, and 2.4~2.6 is the  $D_S$  range (Figure 4). It can be concluded that the  $D_S$  of type B is lower than that of type A, and the PFDH of type B is lower than that of type A. The results of this model are different from those of the *M* model, because the *M* model represents the complexity of the surface area, while the *S* model represents the roughness of the pore volume, in which the *M* model represented the complexity of the surface area, while the *S* model represented the roughness of the pore volume.

Figure 5 indicates that the  $q \sim D(q)$  of samples exhibits a distinct inverse S shape, indicating a multifractal pattern in the pore distribution (Equation (3)) and highlighting the heterogeneous nature of the pore structure. The range of  $D_{-10} \sim D_0$  for type A is 0.5~1.2, and the range of  $D_0 \sim D_{10}$  is 0.1~0.3. The range of  $D_{-10} \sim D_0$  for type B is 0.6~1.0, and the range of  $D_0 \sim D_{10}$  is 0.4~0.5. According to the literature, the heterogeneity in the region of low-pore-volume values corresponds to the left spectral width, whereas the heterogeneity in the region of high-pore-volume values corresponds to the right spectral width. On the left side of the curve is greater than type B, and type A on the micro-pore volume distribution has strong heterogeneity. The type B curve on the right side is greater than type A, and the type-B macro-pore volume distribution heterogeneity is strong.

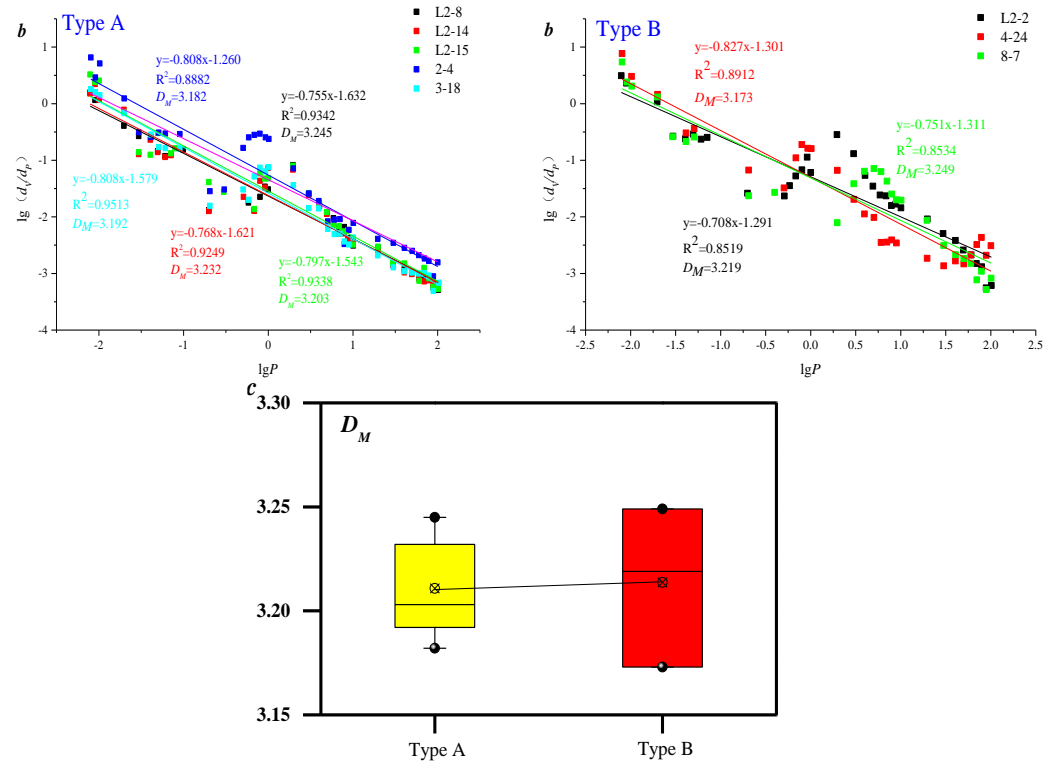


**Figure 3.** Comparison of different types of fractal dimensions based on *M* model ((a), fractal curves of type A; (b), fractal curves of type B; (c), fractal dimension of type A and B).

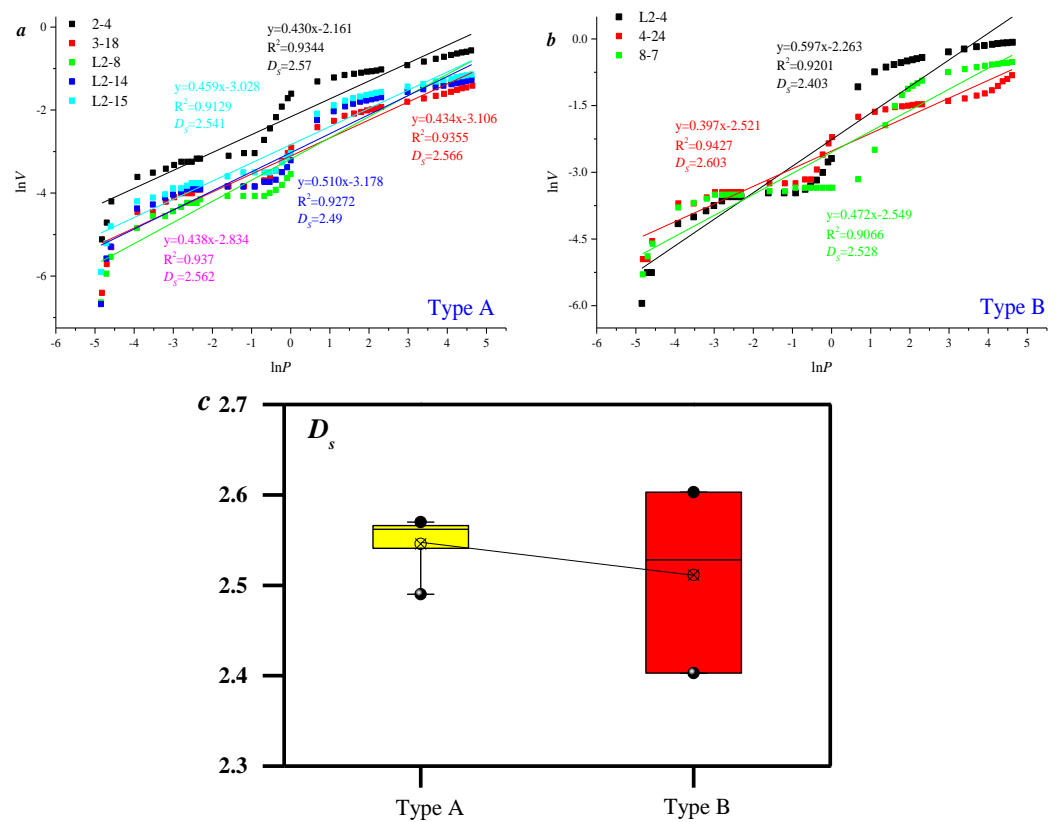


**Figure 4.** Comparison of fractal dimensions of different types of *S* models ((a), fractal curves of type A; (b), fractal curves of type B; (c), fractal dimension of type A and B).

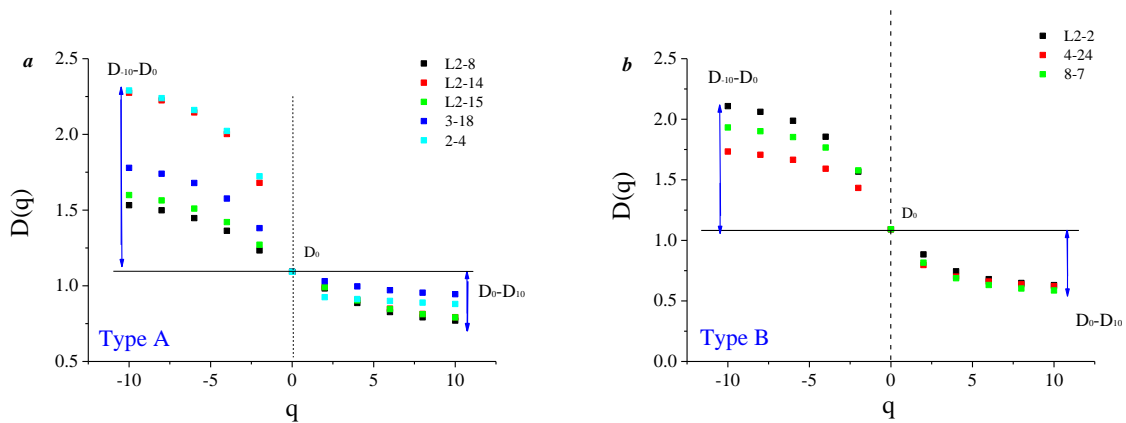


**Figure 5.** Different samples of multifractals are compared during the mercury injection phase ((a), fractal curves of type A; (b), fractal curves of type B).

As can be seen from Figure 6, 0.4–1.2 is the range of  $D_{-10}-D_0$  for type-A adsorption pores, and 0.5–1.0 is the range of  $D_{-10}-D_0$  for type-B adsorption pores. It can be concluded that the heterogeneity of type-A adsorption pores is strong, which is the same as the result in Figure 6. The  $D_0-D_{10}$  of class A is between 0.1 and 0.4, and the  $D_0-D_{10}$  of class B is between 0.4 and 0.6, indicating that the macro-pore heterogeneity of class B is significant, and this result is also the same as that in Figure 6.

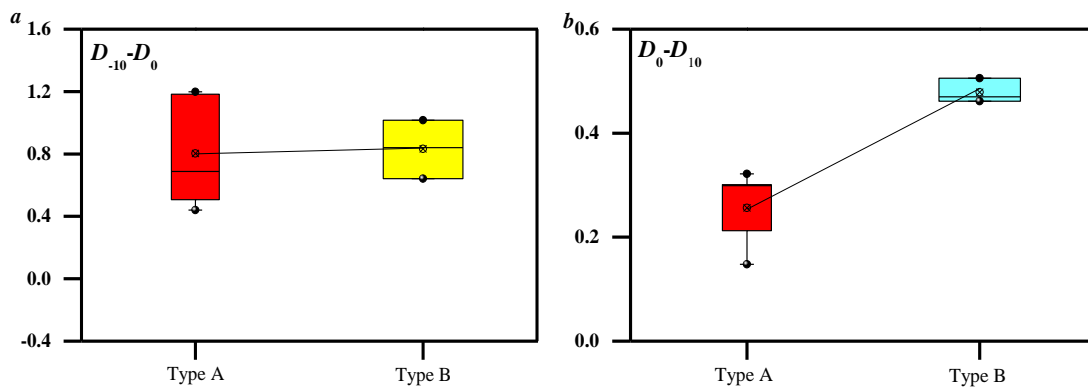
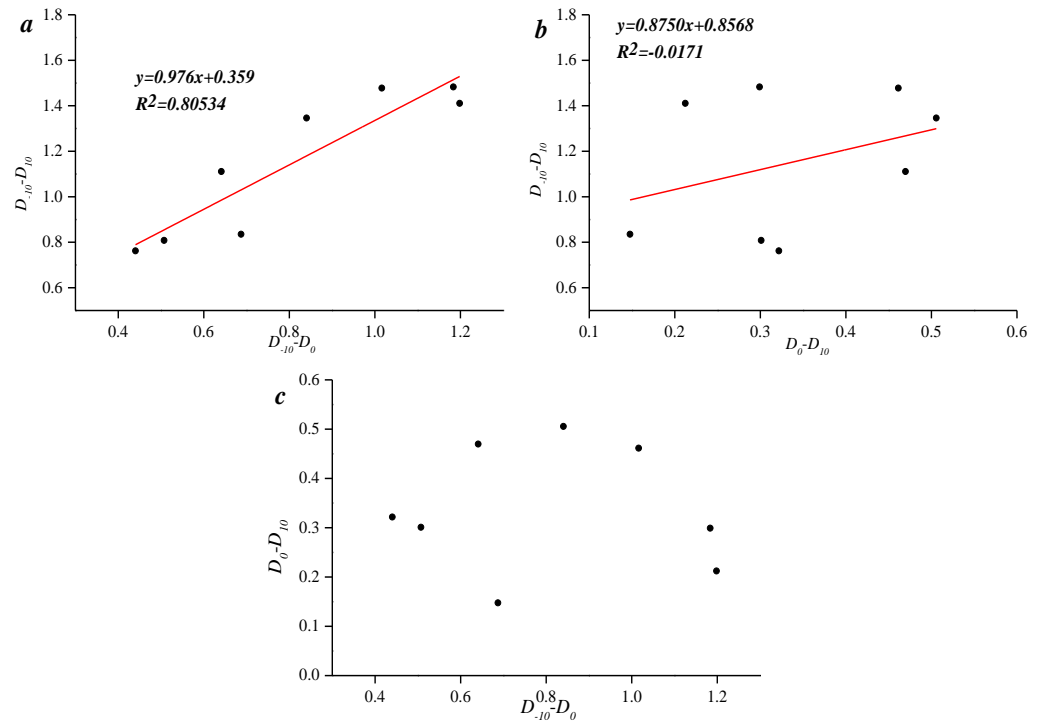


**Figure 6.** The multifractality of all samples in the mercury injection stage was compared ((a),  $D_{-10}-D_0$  variation of type A and B; (b),  $D_0-D_{10}$  of type A and B).

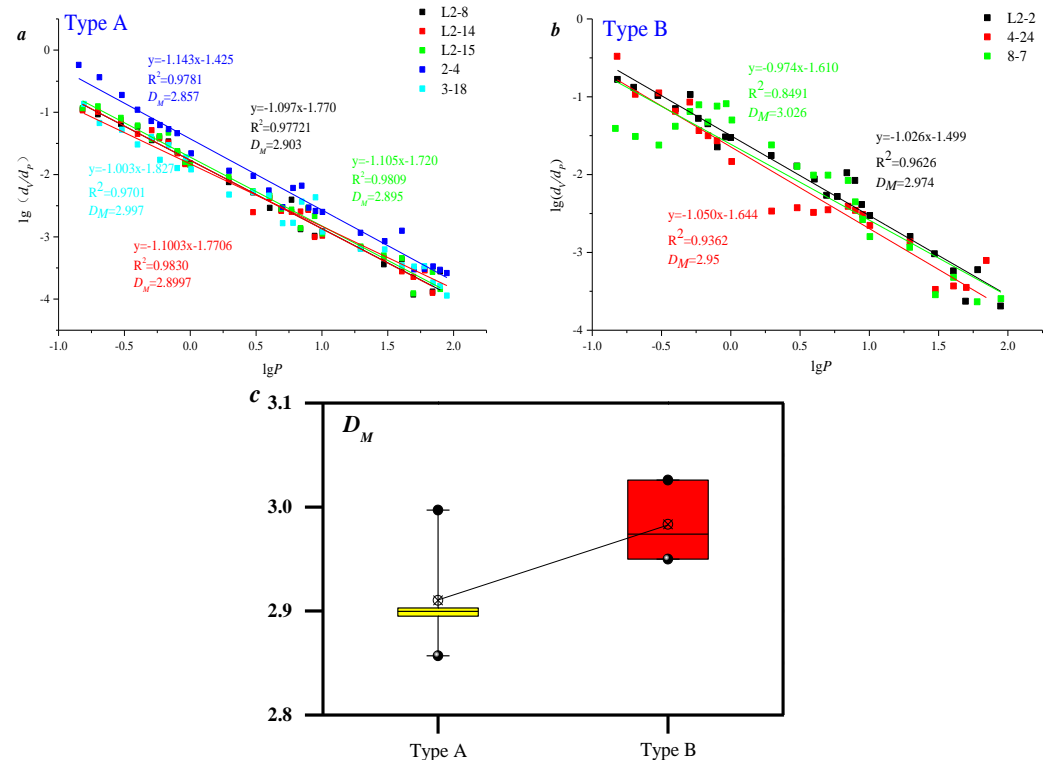
The multifractal results indicate that there is a positive correlation between  $D_{-10}-D_0$  and  $D_0-D_{10}$ , and there is no linear relationship between  $D_{-10}-D_0$  and  $D_{-10}-D_{10}$ , indicating that PFDH is influenced by the low-pore-volume area (Figure 7), as there is a positive correlation between  $D_{-10}-D_0$  and  $D_{-10}-D_{10}$ , and there is a linear relationship between  $D_0-D_{10}$  and  $D_{-10}-D_{10}$ , indicating that PFDH is influenced by the higher-pore-volume area (Figure 7).

### 3.3. Quantitative Description of Heterogeneity of Pore and Fracture Distribution Based on Mercury Removal Curves

$D_M$  can be obtained using the Menger model calculation (Equation (1)). The negative linear correlation between  $\log p$  and  $\log (dv/dp)$  can be reflected by the fractal curve, so it can be shown that the MRC sample has fractal characteristics. The range of 0.97 to 0.98 is the linear fitting range of class A, and 2.85 to 2.99 is the  $D_M$  range. The range of 0.84 to 0.96 is the linear fitting range of class B, and 2.95 to 3.02 is the  $D_M$  range (Figure 8). The  $D_M$  of type B is comparatively higher than that of type A, indicating a stronger PFDH in type B compared to type A.



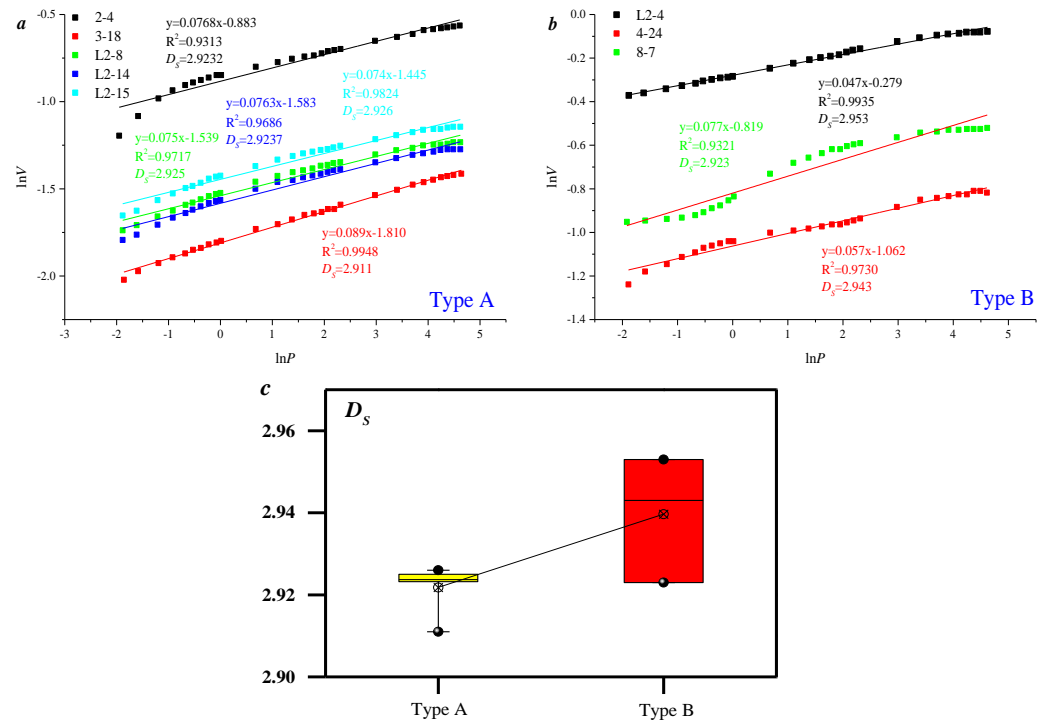
**Figure 7.** Multifractals of all samples in the mercury injection stage were compared ((a),  $D_{-10}-D_0$  vs.  $D_{-10}-D_{10}$ ; (b),  $D_0-D_{-10}$  vs.  $D_{-10}-D_{10}$ ; (c),  $-D_{10}-D_0$  vs.  $D_{-10}-D_0$ ).



**Figure 8.** The fractal dimensions of various samples are compared using the  $M$  model ((a), fractal curves of type A; (b), fractal curves of type B; (c), fractal dimension of type A and B).

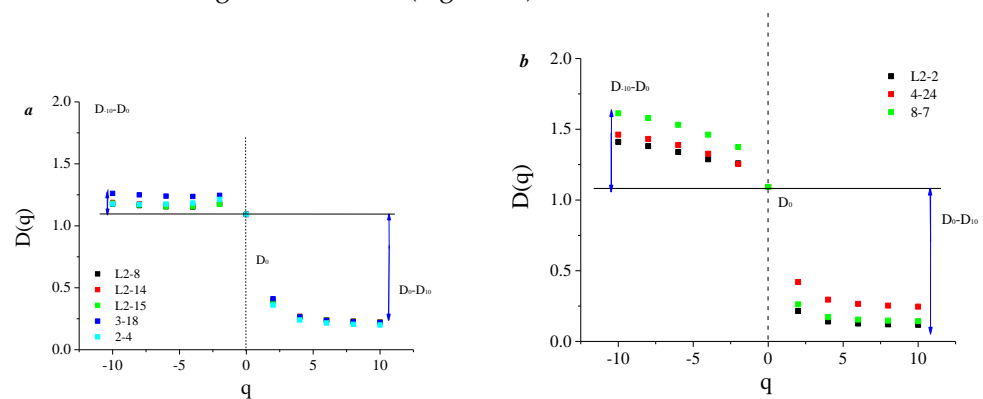
The Sierpinski model can be used to calculate the  $D_5$  (Equation (2)). The linear positive correlation between  $\ln v$  and  $\ln p$  can be reflected by the fractal curve, which indicates that the model can reflect the fractal of MRC. The range of 0.93 to 0.99 is the linear fitting range of class A, and 2.91 to 2.92 is the  $D_5$  range. The range of 0.93 to 0.99 is the linear fitting range

of class B, and 2.92 to 2.95 is the  $D_S$  range (Figure 9). The comparison reveals that the  $D_S$  of type A is lower than that of type B, consistent with Figure 9 but not with Figure 4. This inconsistency underscores the reliability of the results obtained from the MRC-based fractal model.



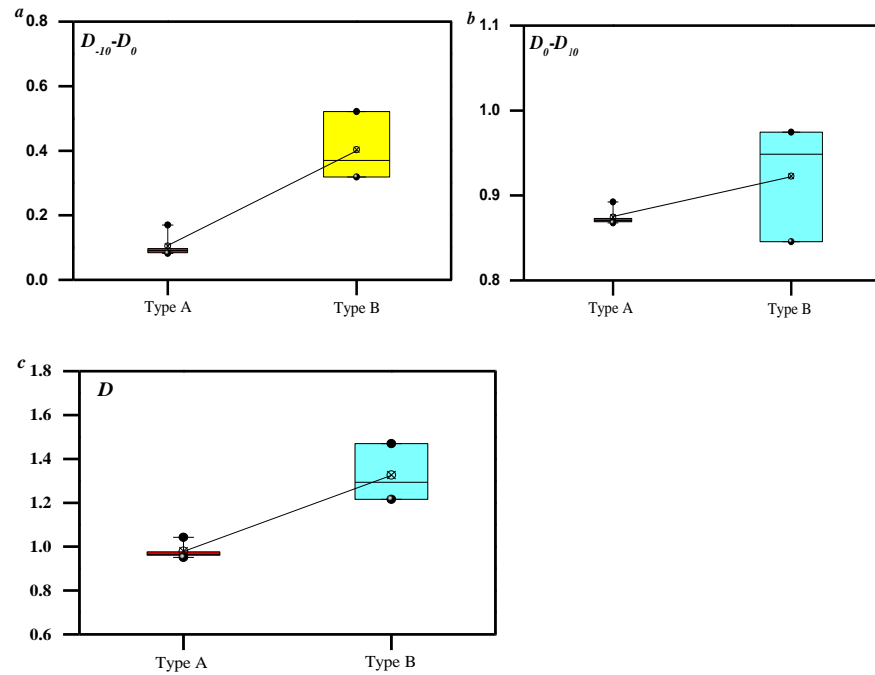
**Figure 9.** Comparison of the fractal dimension of different samples based on the S model ((a), fractal curves of type A; (b), fractal curves of type B; (c), fractal dimension of type A and B).

$Q \sim D(q)$  is inverse S for all samples, showing that the MRC-based pore distribution also has multifractal features. The range of  $D_{-10} - D_0$  for type A is 0.08~0.16, and the range of  $D_0 - D_{10}$  is 0.86~0.89. The range of  $D_{-10} - D_0$  for type B is 0.31~0.52, and the range of  $D_0 - D_{10}$  is 0.84~0.97. According to the literature, the heterogeneity in the low-value-pore-volume region corresponds to the left spectral width, while the heterogeneity in the high-value-pore-volume region corresponds to the right spectral width. The curve on the left side of type B is larger than that of type A, indicating that type B exhibits pronounced heterogeneity in the distribution of the micro-pore volume. Conversely, the curve on the right side of type B is larger than that of type A, suggesting that type B displays significant heterogeneity in the distribution of the large pore volume. This observation contrasts with our understanding based on MIC (Figure 10).

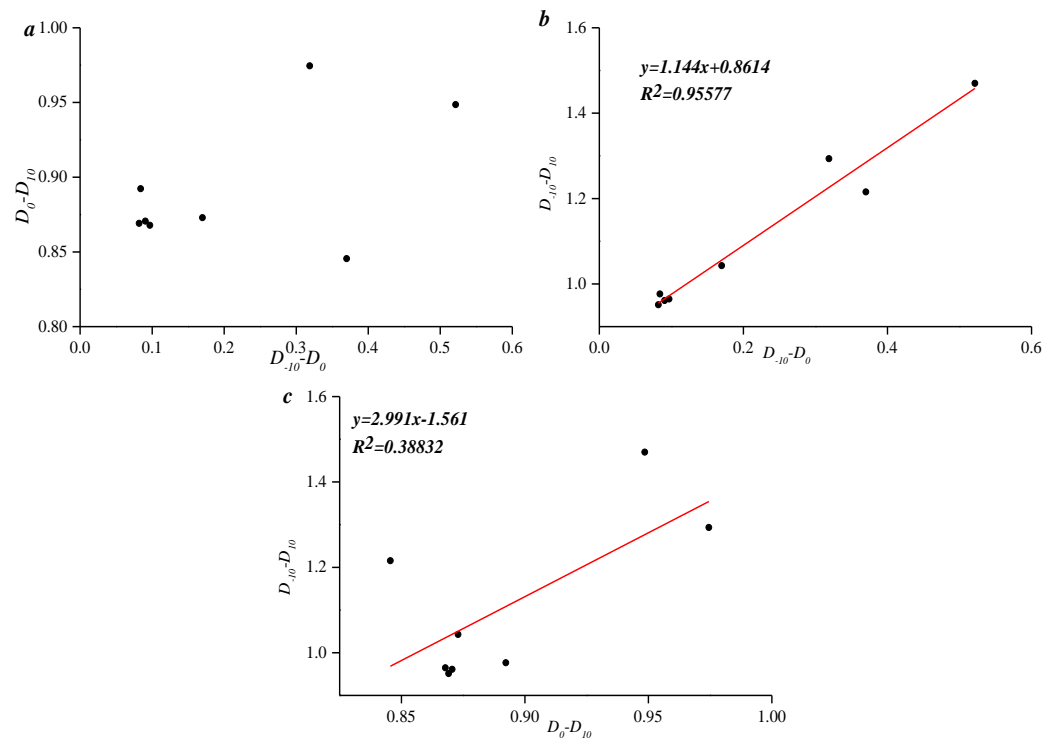


**Figure 10.** Multifractal sample pores based on mercury removal curve ((a), fractal curves of type A; (b), fractal curves of type B).

Figure 11 shows that the  $D_{-10}-D_0$  range of type A is between 0.08 and 0.16, and  $D_{-10}$ -the  $D_0$  range of type B is between 0.31 and 0.52, which indicates that type B has strong heterogeneity of micro-pores and meso-pores, which is consistent with the results in Figure 12. The  $D_0\sim D_{10}$  range of type A is 0.86~0.89, and the  $D_0\sim D_{10}$  range of type B is 0.84~0.97. According to this result, the heterogeneity of medium and large pores of type B is more significant.



**Figure 11.** Multifractal sample based on mercury withdrawal curve ((a), fractal curves of type A; (b), fractal curves of type B; (c), fractal dimension of type A and B).



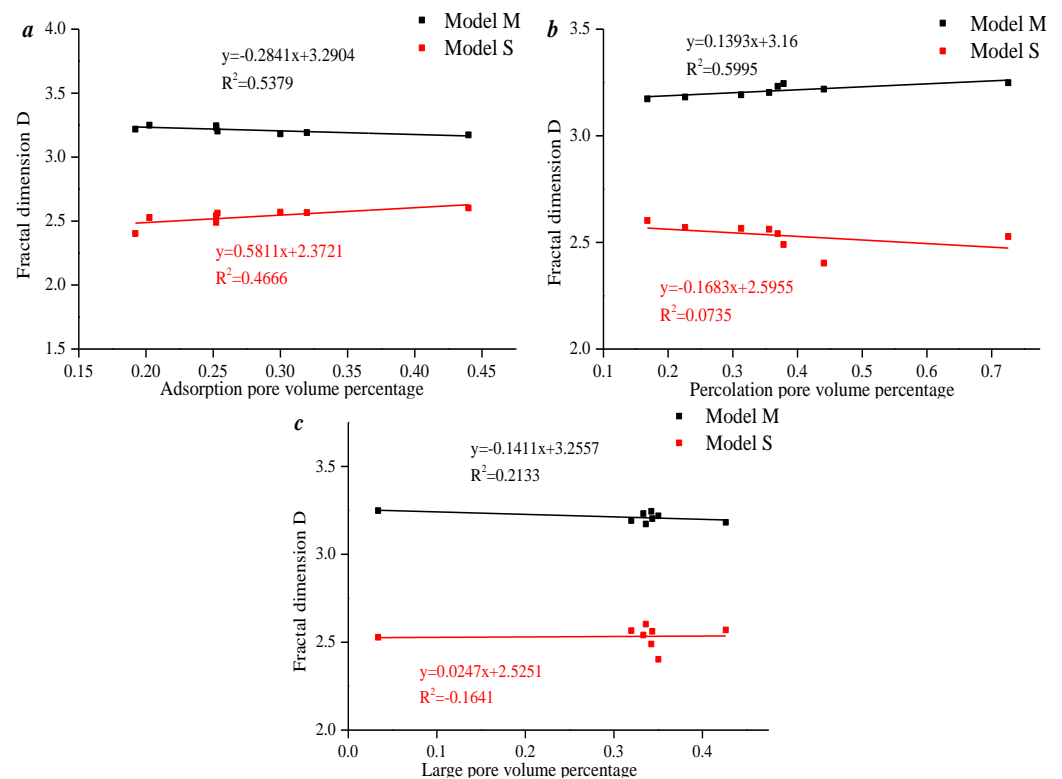
**Figure 12.** Multifractal parameters of all samples were compared according to the mercury removal curve (a), fractal curves of type A; (b), fractal curves of type B; (c), fractal dimension of type A and B.

Figure 12 shows that  $D_{-10}-D_0$  and  $D_{-10}-D_{10}$  were positively correlated and  $D_{-10}-D_0$  and  $D_{-10}-D_{10}$  were positively correlated, and there was a wireless relationship between  $D_0-D_{10}$  and  $D_{-10}-D_{10}$  and between  $D_{-10}-D_0$  and  $D_0-D_{10}$ .

### 3.4. The Influencing Factors the Pore Fractal Characteristics and Applicability Analysis

According to Figure 13a, the percentage of the adsorption pore volume is positively correlated with  $D_M$  and  $D_S$ , and it can be concluded that the percentage of the adsorption pore volume can reflect the PFDH. Figure 13b shows that the percentage of the pore volume in percolation is positively correlated with  $D_M$  and has no correlation with  $D_S$ , indicating that the  $M$  model should be adopted to characterize the PFDH of percolation. Figure 14c shows that the percentage of the macro-pore volume has a weak relationship with  $D_M$  and  $D_S$ , but the linear relationship between  $D_M$  and the macro-pore volume percentage is stronger than  $D_S$ , indicating that the  $M$  model should be used to characterize the PFDH of macro-pores. In summary,  $D_M$  has a relationship with the pore volume percentage at different stages, so the  $M$  model can better characterize PDFH at the mercury inlet stage.

Figure 14a indicates that the percentage of pore volume has a weak positive linear correlation with both  $D_S$  and  $D_M$ , indicating that the micro-pore volume percentage can reflect PDFH in the  $S$  and  $M$  models. Figure 14b shows that the percentage of the seepage pore volume is weakly correlated with  $D_M$ , while there is no significant correlation with  $D_S$ , showing that the  $M$  model should be used to characterize the PFDH of percolation. Figure 14c shows that the percentage of the macro-pore volume is negatively correlated with  $D_M$  and has no linear relationship with  $D_S$  and  $D_T$ . It can be concluded that the  $M$  model should be used to characterize the PFDH of macro-pores. In summary,  $D_M$  has a significant relationship with the pore volume percentage in different stages, so the  $M$  model in the mercury removal stage can better characterize PDFH.



**Figure 13.** Pore volume based on mercury import curve parameters and the correlation analysis of fractal dimension ((a), fractal dimension vs. adsorption volume; (b), fractal dimension vs. seepage pore volume; (c), fractal dimension vs. larger pore volume).

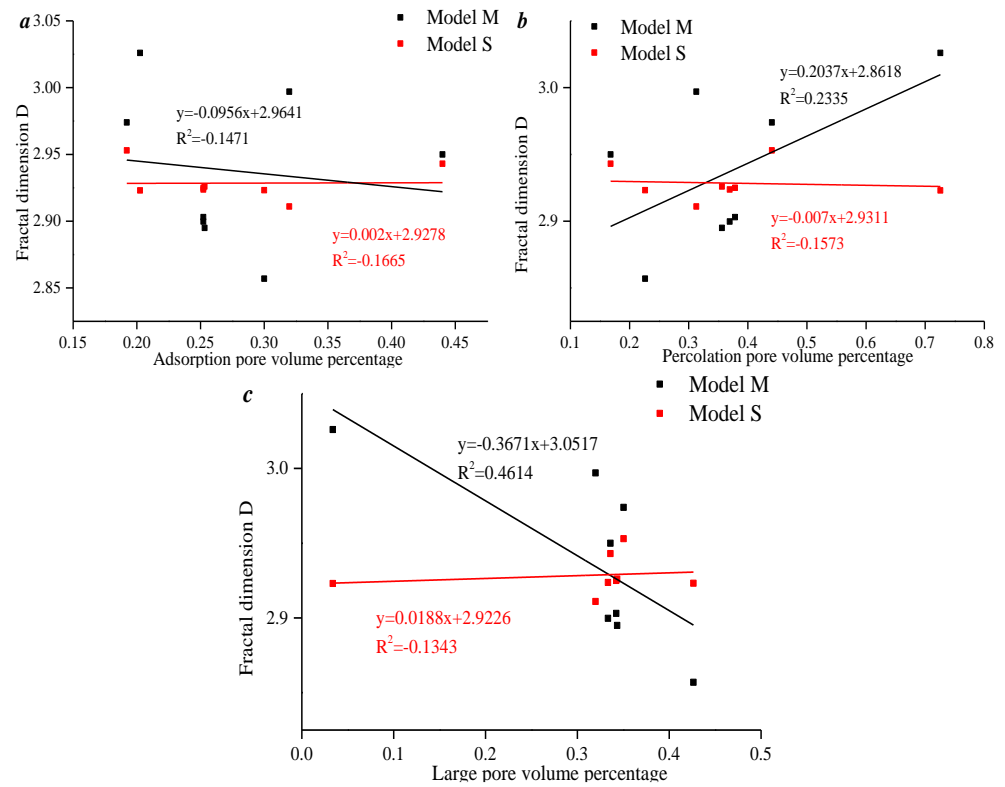


**Figure 14.** The pore volume to take off the mercury curve parameters and the correlation analysis of fractal dimension ((a), fractal dimension vs. adsorption volume; (b), fractal dimension vs. seepage pore volume; (c), fractal dimension vs. larger pore volume).

There is a weak correlation between  $D_{M1}$  based on the mercury intake phase and  $D_{M2}$  derived from the mercury withdrawal phase. A weak correlation is found between  $D_{S1}$  based on the mercury inlet stage and  $D_{S2}$  based on the mercury removal stage, indicating that the physical significance of the M model and the S model is different in the study of MIC and MRC fractal characteristics (Figure 15).

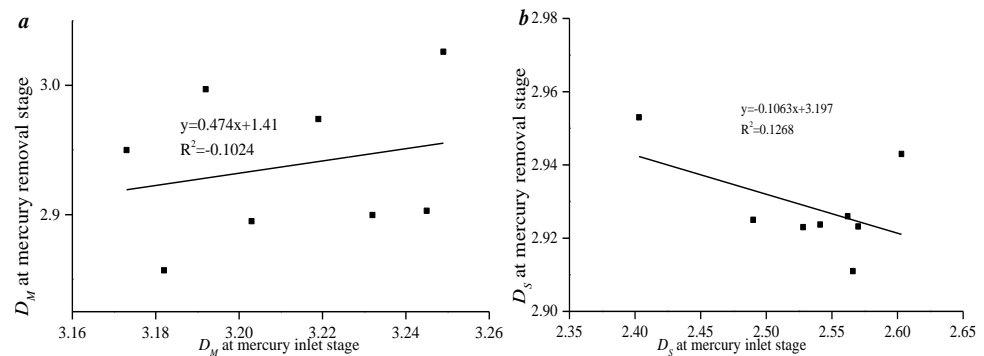


**Figure 15.** Correlation between the fractal dimension of mercury inflow and mercury withdrawal ((a), fractal dimension vs. adsorption volume; (b), fractal dimension vs. seepage pore volume).

There is no significant relationship between  $D_{10}$ ,  $D_{-10}$ ,  $D_{-10}-D_0$ ,  $D_0-D_{10}$ ,  $D_{-10}-D_{10}$ , and  $D_{-10}/D_{10}$  based on the mercury injection stage and mercury removal stage. Different from the single fractal parameters, unlike the single fractal parameters, the correlation among multifractal parameters is weak under both MIC and MRC conditions. This suggests that the physical significance elucidated by multifractal parameters based on MRC differs from that of MIC (Figure 16).

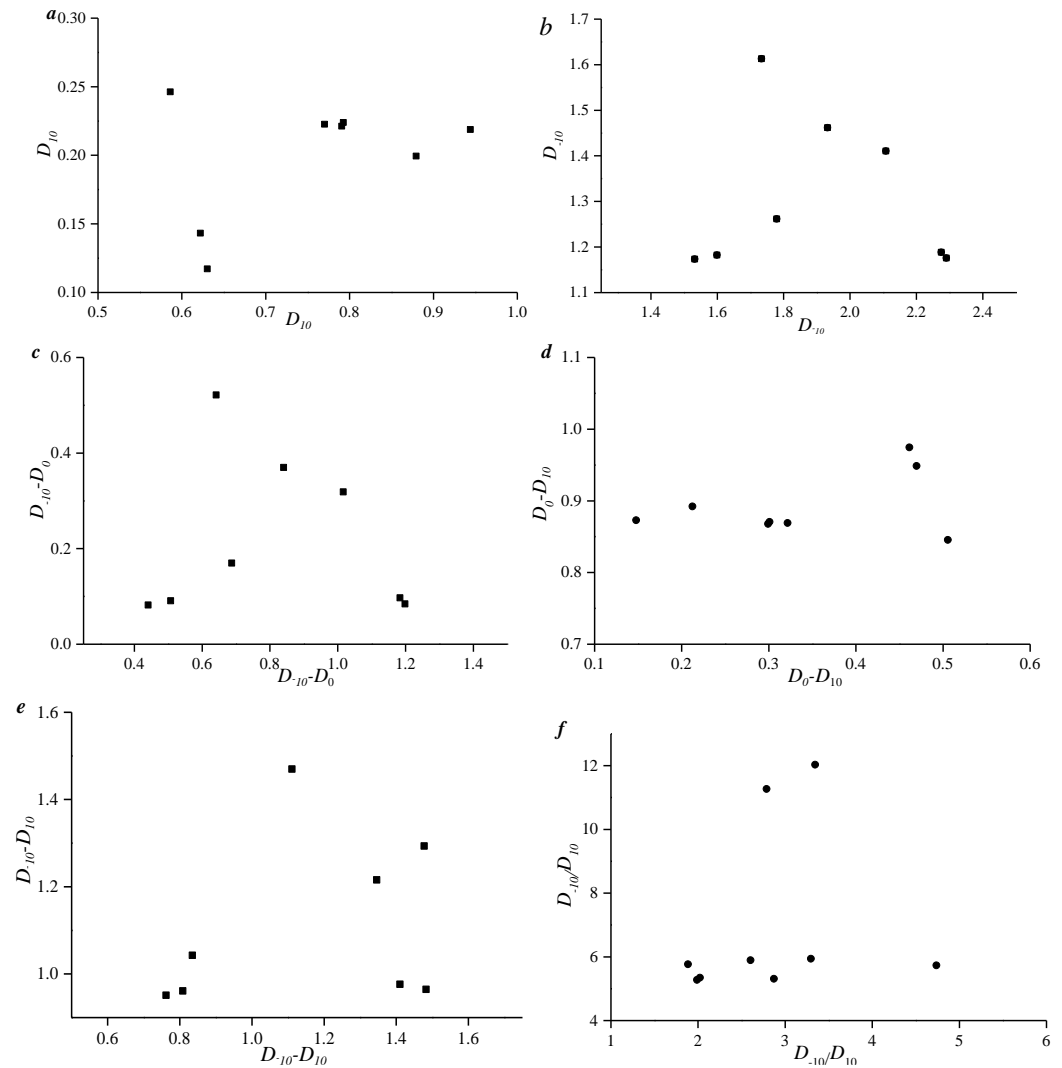


**Figure 16.** Multifractal parameter relationships based on mercury inlet curve and mercury removal curve ((a),  $D_{10}$  of intrusive vs.  $D_{10}$  of removal curves. (b),  $D_{-10}$  of intrusive vs.  $D_{-10}$  of removal curves. (c),  $D_{-10}-D_0$  of intrusive vs.  $D_{-10}-D_0$  of removal curves. (d),  $D_{-10}-D_{10}$  of intrusive vs.  $D_{-10}-D_{10}$  of removal curves. (e),  $D_{-10}-D_{10}$  of intrusive vs.  $D_{-10}-D_{10}$  of removal curves. (f),  $D_{-10}/D_{10}$  of intrusive vs.  $D_{-10}/D_{10}$  of removal curves).

#### 4. Conclusions

Many studies have used fractal theory to characterize pore structure distribution heterogeneity through mercury intake curves. However, there is relatively little research on the fractal model calculation of mercury removal curves. In this study, HPMI is used to describe the pore and fracture distribution in shale reservoirs. MIC and MRC are calculated using single and multifractal models, and the suitability of different fractal models for characterizing PFDH is examined. Furthermore, the physical interpretation of the mercury removal fractal dimension can be inferred from the correlation between the mercury intake fractal dimension and the mercury removal fractal dimension. The conclusions drawn from this study are outlined as follows.

- (1) Based on the mercury removal efficiency and porosity, the samples can be divided into two types: type A (mercury removal efficiency above 35%) and type B (mercury removal efficiency below 35%). Generally, type A belongs to micro-pore-developed types, while type B belongs to macro-pore-developed types.
- (2) The M model indicates that the pore-filling desorption hysteresis (PFDH) of type A and type B is consistent, whereas the S model shows that the PFDH of type A is

significantly stronger than that of type B. This difference can be attributed to the fact that the M model represents the complexity of the specific surface area, while the S model represents the roughness of the pore volume. A positive correlation was found between  $D_{-10}-D_0$  and  $D_{-10}-D_{10}$ , indicating that PFDH is influenced by the low-pore-volume region, whereas there was no correlation between  $D_0-D_{10}$  and  $D_{-10}-D_{10}$ . PFDH affects the storage characteristics of coalbed methane. By studying the PFDH, it is possible to evaluate the reserves and distribution patterns. Coalbed methane undergoes gas migration within the coal body through adsorption and desorption, and the PFDH can affect the path and velocity of gas migration within the coal. Studying the PFDH helps to gain a deeper understanding of the migration patterns of gases, guiding the extraction of coalbed methane and improving mining efficiency.

- (3) Different from the mercury intrusion curves (MICs), the calculation results of the mercury retention curves (MRCs) based on two single fractal models indicate that the pore-filling desorption hysteresis (PFDH) of type B is stronger than that of type A. Additionally, the multifractal characteristics of MRC differ from those of MIC, indicating that the fractal characteristics of MRC are distinct from those of MIC. The mercury migration curve reflects the adsorption, desorption, and migration processes of gases in pores. Understanding the migration patterns and characteristics of gas in coal seams is of significance for guiding the extraction process of coalbed methane. By studying the advance and retreat mercury curves, we can understand the migration patterns of gases under different pore structures, guide the layout of mining wells and the adjustment of mining parameters, and improve the efficiency of coalbed methane extraction.
- (4) The relationship between  $D_M$  and the pore volume percentage at different stages suggests that the M model can better characterize the pore-filling desorption hysteresis (PFDH) at the mercury inlet stage. Similarly, the results of the mercury removal fractal calculation indicate that  $D_M$  also has a relationship with the pore volume percentage at different stages, further supporting the idea that the M model can better characterize PFDH at the mercury removal stage.

**Author Contributions:** J.Z. and H.C.: Writing—Original draft, Experimental methods. P.Y. and D.X.: Conceptualization, Writing—Reviewing and Editing. D.W.: Visualization, Investigation. V.V.: Software, Validation. J.Z.: Experimental methods. X.L.: Writing—Reviewing and Editing. All authors have read and agreed to the published version of the manuscript.

**Funding:** This research was sponsored by the Natural Science Foundation of Shandong Province, China (Nos. ZR2021QD072 and ZR2020QD040).

**Data Availability Statement:** Data are contained within the article.

**Conflicts of Interest:** Author Huasheng Chong was employed by the company Tengzhou Guozhuang Mining Co., Ltd. The remaining authors declare that the research was conducted in the absence of any commercial or financial relationships that could be construed as a potential conflict of interest. The company had no role in the design of the study; in the collection, analyses, or interpretation of data; in the writing of the manuscript, or in the decision to publish the results.

## References

1. Lou, Y.; Su, Y.; Gao, W.; Wang, W.; Xiong, W.; Chen, J.; Xia, P. Pore characteristics and fractal characterization variability of typical middle- and high-rank coal reserves: A case study of middle- and high-rank coal samples in western Guizhou. *Front. Energy Res.* **2022**, *10*, 981530. [[CrossRef](#)]
2. Deng, J.; Zhao, J.; Huang, A.; Zhang, Y.; Wang, C.; Shu, C. Thermal behavior and microcharacterization analysis of second-oxidized coal. *J. Therm. Anal. Calorim.* **2017**, *127*, 439–448. [[CrossRef](#)]
3. Li, J.; Lu, S.; Cai, Y.; Xue, H.; Cai, J. Impact of coal ranks on dynamic gas flow: An experimental investigation. *Fuel* **2017**, *194*, 17–26. [[CrossRef](#)]
4. Niu, C.; Xia, W.; Xie, G. Effect of low-temperature pyrolysis on surface properties of sub-bituminous coal sample and its relationship to flotation response. *Fuel* **2017**, *208*, 469–475. [[CrossRef](#)]
5. Li, Y.; Zhang, C.; Tang, D.; Gan, Q.; Niu, X.; Wang, K.; Shen, R. Coal pore size distributions controlled by the coalification process: An experimental study of coals from the Junggar, Ordos and Qinshui basins in China. *Fuel* **2017**, *206*, 352–363. [[CrossRef](#)]
6. Hodot, B.B. *Outburst of Coal and Coalbed Gas (Chinese Translation)*; China Industry Press: Beijing, China, 1966.

7. IUPAC (International Union of Pure and Applied Chemistry). Physical chemistry division commission on colloid and surface chemistry, subcommittee on characterization of porous solids: Recommendations for the characterization of porous solids (technical report). *Afr. J. Pure Appl. Chem.* **1994**, *66*, 1739–1758. [[CrossRef](#)]
8. Tatsumi, K.; Corish, J. Name and symbol of the element with atomic number 112 (IUPAC Recommendations 2010). *Pure Appl. Chem.* **2010**, *82*, 753–755. [[CrossRef](#)]
9. Wang, C.; Cheng, Y. Role of coal deformation energy in coal and gas outburst: A review. *Fuel* **2023**, *332*, 126019. [[CrossRef](#)]
10. Zhao, J.; Tian, S.; Zou, Q.; Xie, H.; Ran, Q.; Ma, T.; Zhang, X. Effect of SiO<sub>2</sub>-H<sub>2</sub>O nanofluids on wettability of pulverized coal and the modification mechanism. *Fuel* **2024**, *359*, 130396. [[CrossRef](#)]
11. Zhao, J.; Tian, S.; Li, P.; Xie, H.; Cai, J. Molecular dynamics simulation and experimental research on the influence of SiO<sub>2</sub>-H<sub>2</sub>O nanofluids on wettability of low-rank coal. *Colloids Surf. A Physicochem. Eng. Asp.* **2023**, *679*, 132580. [[CrossRef](#)]
12. Zhou, S.; Liu, D.; Cai, Y.; Karpyn, Z.; Yao, Y. Comparative analysis of nanopore structure and its effect on methane adsorption capacity of Southern Junggar coalfield coals by gas adsorption and FIB-SEM tomography. *Microporous Mesoporous Mater.* **2018**, *272*, 117–128. [[CrossRef](#)]
13. Ling, L.Q.; Xin, S.P.; Zhao, F.W.; Xiang, J.C.; Ju, H.D. Study on the Pore Structures and Adsorption Characteristics of Coking Coal of Liulin Mining in China Under the Condition of High Temperature and High Pressure. *Front. Earth Sci.* **2022**, *10*, 877462. [[CrossRef](#)]
14. Guo, S.; Cao, Y.; Zhang, J.; Zhang, X.; Meng, B.; Liu, S. Pore-Microfracture Structure Alteration of Coal Induced by High-Pressure CO<sub>2</sub> Gas Fracturing. *Energy Fuels* **2023**, *37*, 4341–4348. [[CrossRef](#)]
15. Wei, P.; Liang, Y.; Zhao, S.; Peng, S.; Li, X.; Meng, R. Characterization of Pores and Fractures in Soft Coal from the No. 5 Soft Coalbed in the Chenghe Mining Area. *Processes* **2019**, *7*, 13. [[CrossRef](#)]
16. Liu, M.; Xie, R.; Li, C.; Li, X.; Jin, G.; Guo, J. Determining the segmentation point for calculating the fractal dimension from mercury injection capillary pressure curves in tight sandstone. *J. Geophys. Eng.* **2018**, *15*, 1350–1362. [[CrossRef](#)]
17. Zhang, X.; Liu, C.; Nepal, S.; Yang, C.; Dou, W.; Chen, J. A hybrid approach for scalable sub-tree anonymization over big data using MapReduce on cloud. *J. Comput. Syst. Sci.* **2014**, *80*, 1008–1020. [[CrossRef](#)]
18. Yue, G.; Liu, H.; Yue, J.; Li, M.; Liang, W. Influence radius of gas extraction borehole in an anisotropic coal seam: Underground in-situ measurement and modeling. *Energy Sci. Eng.* **2019**, *7*, 694–709. [[CrossRef](#)]
19. Zhao, B.; Yi, H.; Tang, X.; Li, Q.; Liu, D.; Gao, F. Copper modified activated coke for mercury removal from coal-fired flue gas. *Chem. Eng. J.* **2016**, *286*, 585–593. [[CrossRef](#)]
20. Mei, J.; Wang, C.; Kong, L.; Liu, X.; Hu, Q.; Zhao, H.; Yang, S. Outstanding Performance of Recyclable Amorphous MoS<sub>3</sub> Supported on TiO<sub>2</sub> for Capturing High Concentrations of Gaseous Elemental Mercury: Mechanism, Kinetics, and Application. *Environ. Sci. Technol.* **2019**, *53*, 4480–4489. [[CrossRef](#)]
21. Wang, G.; Shen, J.; Liu, S.; Jiang, C.; Qin, X. Three-dimensional modeling and analysis of macro-pore structure of coal using combined X-ray CT imaging and fractal theory. *Int. J. Rock Mech. Min. Sci.* **2019**, *123*, 1040–1082. [[CrossRef](#)]
22. Zhang, J.; Wei, C.; Chu, X.; Vandeginste, V.; Ju, W. Multifractal Analysis in Characterizing Adsorption Pore Heterogeneity of Middle- and High-Rank Coal Reservoirs. *ACS Omega* **2020**, *5*, 19385–19401. [[CrossRef](#)] [[PubMed](#)]
23. Zhang, H.; Xiao, R.; Huang, H.; Xiao, G. Comparison of non-catalytic and catalytic fast pyrolysis of corncob in a fluidized bed reactor. *Bioresour. Technol.* **2009**, *100*, 1428–1434. [[CrossRef](#)] [[PubMed](#)]
24. Hui, S.; Lv, Y.; Niu, Y.; Kan, H.; Wang, D.; Li, P. Experimental comparative study on ash fusion characteristics of Ningdong coal under oxidizing and reducing atmosphere by means of SiO<sub>2</sub>-Al<sub>2</sub>O<sub>3</sub>-(CaO + MgO + Na<sub>2</sub>O + K<sub>2</sub>O) pseudo-ternary diagrams. *Fuel* **2019**, *258*, 116–137. [[CrossRef](#)]
25. Kashif, M.; Cao, Y.; Yuan, G.; Asif, M.; Javed, K.; Mendez, J.N.; Khan, D.; Miruo, L. Pore size distribution, their geometry and connectivity in deeply buried Paleogene Es1 sandstone reservoir, Nanpu Sag, East China. *Pet. Sci.* **2019**, *16*, 981–1000. [[CrossRef](#)]
26. Otalvaro, I.F.; Neto, M.P.C.; Delage, P.; Caicedo, B. Relationship between soil structure and water retention properties in a residual compacted soil. *Eng. Geol.* **2016**, *205*, 73–80. [[CrossRef](#)]
27. Peng, J.; Han, H.; Xia, Q.; Li, B. Evaluation of the pore structure of tight sandstone reservoirs based on multifractal analysis: A case study from the Kepingtage Formation in the Shuntuoguole uplift, Tarim Basin, NW China. *J. Geophys. Eng.* **2018**, *15*, 1122–1136. [[CrossRef](#)]
28. Zhao, L.; Guanhua, N.; Lulu, S.; Qian, S.; Shang, L.; Kai, D.; Jingna, X.; Gang, W. Effect of ionic liquid treatment on pore structure and fractal characteristics of low rank coal. *Fuel* **2020**, *262*, 116513. [[CrossRef](#)]
29. Zhang, J.; Hu, Y. Comparative Evaluation of Pore Structure Heterogeneity in Low-Permeability Tight Sandstones Using Different Fractal Models Based on NMR Technology: A Case Study of Benxi Formation in the Central Ordos Basin. *Energy Fuels* **2020**, *34*, 13924–13942. [[CrossRef](#)]
30. Zhang, M.; Duan, C.; Li, G.; Fu, X.; Zhong, Q.; Liu, H.; Dong, Z. Determinations of the multifractal characteristics of the pore structures of low-, middle-, and high-rank coal using high-pressure mercury injection. *J. Pet. Sci. Eng.* **2021**, *203*, 108656. [[CrossRef](#)]

**Disclaimer/Publisher's Note:** The statements, opinions and data contained in all publications are solely those of the individual author(s) and contributor(s) and not of MDPI and/or the editor(s). MDPI and/or the editor(s) disclaim responsibility for any injury to people or property resulting from any ideas, methods, instructions or products referred to in the content.